Cryogenics 158 (2026) 104360

Contents lists available at ScienceDirect

Cryogenics

journal homepage: www.elsevier.com/locate/cryogenics

Design of an experimental setup for heat transfer coefficient measurements of supercritical helium for hydrogen aviation applications

Parmit S. Virdi[a,b], Wei Guo[a,b,*], Louis N. Cattafesta III[c], Peter Cheetham[d,e], Lance Cooley[a,b,f], Jonathan C. Gladin[g,h], Jiangbiao He[i], D.M. Ionel[i,j], Chul Kim[e], Hui Li[d,e], Juan Ordonez[a,e], Sastry Pamidi[d,e], Jian-Ping Zheng[j]

[a] *Mechanical Engineering Department, FAMU-FSU College of Engineering, 2525 Pottsdamer St, Tallahassee, Florida 32310, USA*
[b] *National High Magnetic Field Laboratory, 1800 E Paul Dirac, Tallahassee, Florida 32310, USA*
[c] *Illinois Institute of Technology, 10 West 32th Street, Chicago, Illinois 60616, USA*
[d] *Electrical and Computer Engineering Department, FAMU-FSU College of Engineering, 2525 Pottsdamer St, Tallahassee, Florida 32310, USA*
[e] *Center for Advance Power Systems, 2000 Levy Avenue, Tallahassee, Florida 32310, USA*
[f] *Applied Superconductivity Center, 2031 E Paul Dirac Dr, Tallahassee, Florida 32310, USA*
[g] *Daniel Guggenheim School of Aerospace Engineering, Georgia Tech, North Avenue, Atlanta, Georgia 30332, USA*
[h] *Aerospace Systems Design Laboratory, 275 Ferst Drive NW, Atlanta, Georgia 30332, USA*
[i] *Department of Electrical Engineering and Computer Science, University of Tennessee, 1520 Middle Dr, Knoxville, Tennessee 37996, USA*
[j] *Department of Electrical Engineering, University at Buffalo, 230 Davis Hall, University at Buffalo, North Campus, Buffalo, New York 14260, USA*

HIGHLIGHTS

- Identifies missing forced-convection data for supercritical helium at 30–70 K.
- Presents a constraint-based design of a supercritical-helium heat-transfer facility.
- Achieves cryofan-driven helium flow up to Re $\approx 10^6$ at pressures up to 20 bar.
- Enables accurate validation of heat-transfer correlations near the pseudo-critical line.

ARTICLE INFO

Keywords:
Supercritical helium
Heat transfer coefficient
High pressures
Cryogenic temperatures
High reynolds number flows

ABSTRACT

Helium is widely employed as a coolant in engineering applications. In its supercritical state, it eliminates liquid–vapor phase separation and enables stable forced-flow cooling, making it attractive for superconducting devices, fusion reactors, and particle accelerators. In our recent studies on liquid-hydrogen-powered aircraft for Integrated Zero Emission Aviation (IZEA), supercritical helium was identified as the preferred coolant for superconducting generators, motors, power converters, and high-current cables, with operation required in the 30–70 K range at 15–20 bar. Accurate knowledge of its forced-convective heat transfer coefficient under these conditions is essential for designing compact and efficient heat exchangers, yet existing data span only limited pressure, temperature, and Reynolds number ranges. To address this gap, we present the design of an experimental facility for precise measurements of supercritical helium heat transfer coefficient under controlled flow and heating conditions. The system was optimized to balance loop diameter, cryofan performance, cryocooler capacity, sensor resolution, and heating requirements. The final setup circulates helium through a 0.5-inch test section at Reynolds numbers up to 10^6, while sustaining pressures up to 20 bar and temperatures down to 4 K. By directly probing this unexplored parameter space, the platform will generate critical data to reduce uncertainties in correlation-based models and advance cryogenic heat exchanger design for IZEA and various applications beyond it. The measurement approach and instrumentation have been designed to ensure high reliability and repeatability of the collected data. The first experimental dataset generated using this platform will be reported in a subsequent publication.

* Corresponding author at: Mechanical Engineering Department, FAMU-FSU College of Engineering, 2525 Pottsdamer St, Tallahassee, Florida 32310, USA.
Email address: wguo@magnet.fsu.edu (W. Guo).

https://doi.org/10.1016/j.cryogenics.2026.104360
Received 23 January 2026; Received in revised form 31 March 2026; Accepted 11 April 2026
Available online 14 April 2026

Nomenclature

Symbol

A	Heat transfer surface area $[m^2]$
C_p	Specific heat capacity at constant pressure $[J/(kg \cdot K)]$
D	Inner diameter of the circulation loop $[m]$
f	Darcy friction factor [–]
G	Mass flux $[kg/(m^2 \cdot s)]$
h	Convective heat transfer coefficient $[W/(m^2 \cdot K)]$
I	Electrical current supplied to heater $[A]$
k	Thermal conductivity $[W/(m \cdot K)]$
L	Heated length of the test section $[m]$
$\dot{m}$	Mass flow rate $[kg/s]$
Nu	Nusselt number (hD/k) [–]
P	Fluid pressure $[Pa]$
Pr	Prandtl number $(C_p\mu/k)$ [–]
q	Applied wall heat flux $[W/m^2]$
$\dot{Q}$	Heat load or power $[W]$
Re	Reynolds number $(\rho v D/\mu)$ [–]
T	Temperature $[K]$
v	Fluid velocity $[m/s]$
V	Electrical voltage $[V]$
$\dot{V}$	Volumetric flow rate $[m^3/s]$
x	Axial position along test section $[m]$

Greeks

α	Metrology resolution ratio [–]
ΔP	Pressure drop $[Pa]$
ΔT	Temperature difference $[K]$
μ	Dynamic viscosity $[Pa \cdot s]$
ρ	Fluid density $[kg/m^3]$

Subscripts

b	Bulk fluid property
c	Critical point
$cryocooler$	Refrigeration lift capacity
D	Driving heating (frictional dissipation)
$heater$	Applied electrical heat
i	Axial location / discrete index
in	Inlet condition
out	Outlet condition
pc	Pseudo-critical
res	Metrology resolution limit
S	Static parasitic heat load
w	Inner wall property

1. Introduction

Helium is a cryogenic fluid with a normal boiling point of 4.2 K at atmospheric pressure. When operated above its critical point at pressures exceeding $P_c \approx 2.3$ bar and temperatures above $T_c \approx 5.2$ K, helium enters a supercritical state that avoids liquid–vapor separation while offering favorable transport characteristics for forced-flow cooling. This combination makes supercritical helium an effective coolant for high-performance cryogenic systems. It has therefore been widely employed in superconducting technologies including particle accelerators, high-field detectors, fusion devices, and power cables [1–10], where maintaining low and stable operating temperatures is essential for preserving superconductivity under strong magnetic fields and significant thermal loads.

This established role in terrestrial superconducting systems also motivates its adoption in emerging electrified aircraft concepts that require lightweight, high-power-density cryogenic thermal management. One such concept is Integrated Zero Emission Aviation (IZEA), a recently proposed hydrogen-powered turboelectric architecture in which liquid hydrogen serves as both the fuel and the ultimate heat sink [11]. In IZEA, hydrogen from onboard storage is routed through a sequence of heat exchangers before reaching the fuel cells and turboelectric generators, providing a system-level pathway to absorb and transport distributed thermal loads [11]. Within this framework, supercritical helium is proposed as the working fluid in dedicated secondary loops: it extracts heat from superconducting power components (e.g., generators and high-current cables) and transfers that heat to the hydrogen pipeline through compact counterflow heat exchangers [11]. The required operating envelope for these helium loops spans 30–70 K at 15–20 bar, making accurate forced-convection heat-transfer coefficients for supercritical helium essential for heat-exchanger sizing, optimization, and stable operation.

The measurement of heat transfer coefficients h for supercritical fluids has been pursued across diverse engineering sectors, utilizing specific boundary conditions and working gases to address relevant thermal challenges. However, a review of the available literature [12–19] shows that experimental forced-convection heat-transfer measurements for supercritical helium remain sparse and fragmented, covering only limited regions of pressure, temperature, and flow conditions, as shown in Fig. 1. Although several studies report data near ∼ 20 bar, no cohesive dataset spans the temperature range relevant to IZEA systems while simultaneously reaching high Reynolds numbers (Re $\sim 10^6$) and elevated heat fluxes (tens of kW/m^2). Because of this lack of comprehensive data, past IZEA thermal design has relied on semi-empirical correlations. However, widely used “universal” turbulent-convection correlations, such as Dittus–Boelter [20] and Gnielinski [4,21], are not sufficiently reliable for supercritical helium, particularly near the pseudo-critical line, i.e., the locus of temperatures $T_{pc}(P)$ at each pressure P where the specific heat reaches a maximum and related properties (including density and thermal conductivity) vary rapidly. In this regime, the strong property gradients fundamentally alter the convective response in ways that generic correlations do not capture. Consistent with this limitation, comparative assessments of representative correlations [20–27] report systematic over- and under-predictions of the heat-transfer coefficient, with the largest heat-transfer deterioration or enhancement occurring in the pseudo-boiling regime associated with crossing $T_{pc}(P)$.

By contrast, helium-specific correlations, most notably those of Valyuzhinich et al. [18] and Yeroshenko et al. [17,26], achieve improved consistency with the experimental datasets from which they were derived. However, these formulations remain limited by the underlying parameter space of the available measurements, which were largely obtained at lower Reynolds numbers and in smaller-diameter channels than those demanded by modern IZEA-scale hardware. As a result, present-day thermal design of aerospace cryogenic heat exchangers still depends on extrapolation beyond validated ranges, introducing significant uncertainty in predicting convective heat-transfer coefficients, pressure drops, and thermo-hydraulic stability margins under operating conditions. These uncertainties pose a major barrier to the reliable design of compact, lightweight, and high-capacity cryogenic heat exchangers essential for superconducting propulsion and power systems. Addressing this limitation requires new measurements that extend the experimental database into the IZEA regime, enabling correlation development and model validation on a firm foundation.

Beyond helium, extensive data exist for supercritical carbon dioxide sCO_2, hydrogen sH_2, and water SCW. Supercritical carbon dioxide sCO_2: Primarily investigated for power generation cycles, sCO_2 research often employs conjugate heat transfer boundary conditions in horizontal double-pipe heat exchangers or miniature heat sinks [28–30]. Studies in

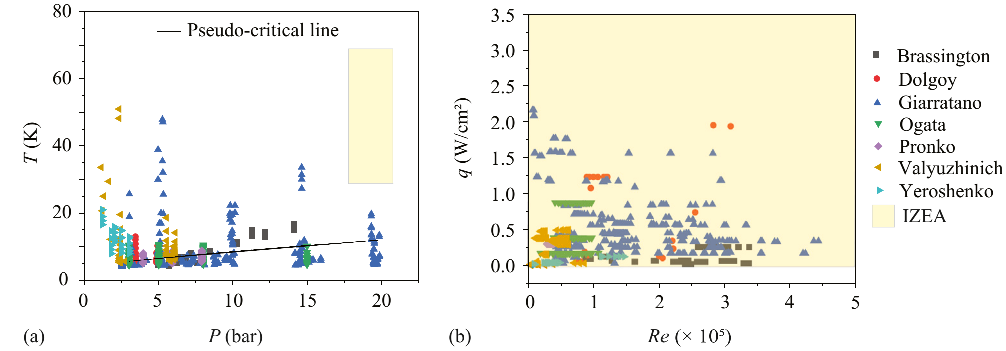

Fig. 1. The plots (a) P vs. T and (b) q vs. Re summarize the existing supercritical-helium heat-transfer database, highlighting how prior measurements are confined to fragmented and limited regions of the operating space. The shaded area denotes the Integrated Zero Emission Aviation (IZEA) target regime, where high-fidelity data are critically needed for design and model validation.

horizontal mini/micro tubes have revealed that buoyancy remains significant even at Reynolds numbers up to 10^5 complicating the isolation of forced-convection effects. In sCO_2 research, aimed primarily at high-efficiency power cycles, measurement errors are typically reported in the 10 percent range, though correlations often deviate by 30–100 percent in the deteriorated heat transfer (HTD) regime. Supercritical Hydrogen (sH2): Fundamental to rocket propulsion and IZEA fuel streams, sH_2 measurements frequently utilize constant heat flux boundary conditions in vertical upward tubes [31]. Supercritical hydrogen studies have focused on extreme heat fluxes (> 10 MW/m^2) for rocket cooling. Results indicate that increasing mass flux can suppress heat transfer deterioration, yet numerical-to-experimental deviations still exceed 10–20% near the pseudo-critical point [32–34]. Supercritical Water: Investigated for high-performance light water reactors, SCW studies focus on extremely high pressures (25 MPa) and temperatures (374 °C). These experiments have established the "pseudo-boiling" theory, treating the fluid as a heterogeneous structure of liquid-like and vapor-like clusters. Two primary boundary conditions dominate the literature: Constant Heat Flux and Constant Wall Temperature. While CHF methods, achieved via resistive heating, allow for precise local determination of h, they are susceptible to localized wall temperature "overshoots".

The present work proposes an experimental facility to generate accurate forced-convection heat-transfer data for supercritical helium under IZEA-relevant conditions and beyond. The facility consists of a forced-flow cryogenic loop that circulates helium to the target Reynolds numbers, precools it to the required temperature range, and applies a well-defined thermal load through controlled electrical heating in a dedicated test section that imposes a uniform heat flux. By precisely regulating P, T, and mass flow rate, and by combining an optimized test-section geometry with high-accuracy instrumentation, the setup enables systematic determination of heat-transfer coefficients in regimes that are not well constrained by existing measurements.

In Section 2, we discuss the experimental concept and overall facility design, while in Section 3 we present the optimized experimental setup and the operating procedure for reaching the maximum achievable Re under constraints set by cryocooler capacity and temperature-sensor resolution. Finally, a brief summary is given in Section 4.

2. Experiment concept and design

2.1. Experiment concept

We implement a closed, circular forced-flow loop in which supercritical helium (SHe) is circulated by a cryofan to reach the target Reynolds number. A cryocooler cold head provides the refrigeration needed to bring the circulating helium into the desired cryogenic temperature range and to hold the inlet conditions stable during a measurement, as illustrated in Fig. 2. The heated test section is integrated into the

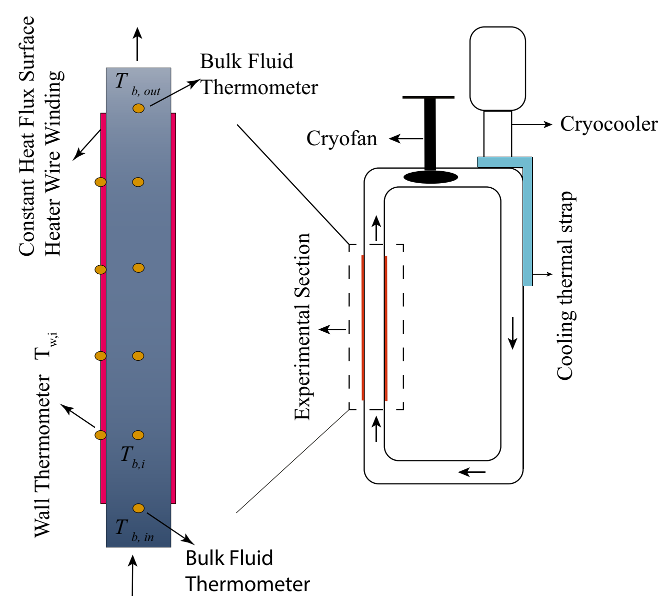

Fig. 2. Experimental concept for forced-convection heat-transfer measurements in supercritical helium (SHe). A cryofan drives circulation in a closed loop to set the desired flow rate (and thus Re), while a cryocooler cold head provides refrigeration to establish and stabilize the inlet temperature. A resistive heater in the test section applies a controlled heat input, producing a measurable bulk-temperature rise between inlet and outlet. Wall and bulk temperatures measured at multiple axial locations are used to determine the local convective heat-transfer coefficient.

loop so that a well-controlled thermal load can be applied under steady, single-phase operating conditions. For each measurement, the loop is first brought to the target operating point (P, T, Re) and allowed to reach steady state. A known electrical heating power $\dot{Q}_{\mathrm{heater}}$ is then deposited over the test-section length L using a resistive heater wire wound on the outer surface of the tube. This produces a controlled increase in the bulk fluid temperature from the test-section inlet $T_{b,\mathrm{in}}$ to the outlet $T_{b,\mathrm{out}}$.

The local forced-convection heat-transfer coefficient h_i at axial station i is obtained from the local wall-to-bulk temperature difference,

$$h_i = \frac{q}{T_{w,i} - T_{b,i}} \tag{1}$$

where $T_{w,i}$ is the measured wall temperature, $T_{b,i}$ is the bulk fluid temperature at the same station, and q is the applied wall heat flux. Assuming the heater delivers a uniform heat input along the test section, the average heat flux is

$$q = \frac{\dot{Q}_{\text{heater}}}{\pi D L} \tag{2}$$

with D the tube inner diameter. The electrical heating power is determined directly from the measured current I and voltage V supplied by the power source, i.e., $\dot{Q}_{\text{heater}} = IV$.

Bulk temperatures at the test-section inlet and outlet, $T_{b,\text{in}}$ and $T_{b,\text{out}}$, are measured using thermometers inserted into the flow through vacuum feedthroughs. The bulk temperature at an intermediate station, $T_{b,i}$, is then determined from an energy balance. In its most general form (important for SHe because C_p varies strongly near $T_{pc}(P)$), the axial evolution is computed using the bulk enthalpy rise,

$$\dot{m}\left(h_{b,i} - h_{b,\text{in}}\right) = \dot{Q}(x_i) \tag{3}$$

where $\dot{Q}(x_i)$ is the heater power deposited from $x = 0$ to $x = x_i$, and $h_{b,i}$ is converted to $T_{b,i}$ at the measured pressure using helium property data. For convenience, when the temperature rise across a segment is sufficiently small, this can be written in the familiar form

$$T_{b,i} = T_{b,\text{in}} + \frac{\dot{Q}(x_i)}{\dot{m} C_p} \tag{4}$$

with C_p evaluated consistently (e.g., at local (P, T)). The mass flow rate $\dot{m}$ is obtained calorimetrically from the overall temperature rise across the heated length, $\dot{m} = \dot{Q}_{\text{heater}}/(h_{b,\text{out}} - h_{b,\text{in}})$, which reduces to

$$\dot{m} \approx \frac{\dot{Q}_{\text{heater}}}{\int_{T_{b,\text{in}}}^{T_{b,\text{out}}} C_p(P,T)\, dT} \tag{5}$$

in terms of C_p.

All measurements are performed under steady-state conditions. The cryocooler must remove not only the net heat added by the test-section heater but also parasitic loads, including static conduction from structural supports and components (e.g., the cryofan housing) and radiative heating from warmer surrounding surfaces. To maintain a stable and well-defined inlet bulk temperature $T_{b,\text{in}}$, a trim heater mounted on the cryocooler cold head is regulated by a temperature controller. This trim heater does not increase the cryocooler capacity; rather, it provides controlled counter-heating so that the cold-head temperature—and therefore the refrigeration delivered to the loop—can be held at a precise setpoint despite variations in parasitic heat loads and operating conditions.

2.2. Design procedure

To achieve the experimental objectives, the circulation loop must be designed to reach the target Reynolds number while satisfying constraints imposed by cryocooler capacity, parasitic heat loads, cryofan flow capability, and temperature-measurement resolution. Following the concept in Fig. 2, we first surveyed commercially available cryogenic hardware. We selected the Cryomech PT420 pulse-tube cryocooler [35], because it provides access to temperatures down to ∼ 4 K while offering comparatively high cooling power across the 10–80 K range. For forced circulation, we considered a range of cryofans from Stirling Cryogenics [36], consistent with the class of cryofans previously recommended for SHe secondary loops in IZEA thermal management [11]. With the cryofan and cryocooler chosen, the key remaining design variable is the circulation-loop diameter, since the tube inner diameter D together with the volumetric flow rate $\dot{V}$, sets the achievable Re number at a given operating pressure P and temperature T.

For any chosen D, we set the heated experimental-section length to $L = 50D$. This allocation provides ∼ $10D$ upstream length for flow stabilization after the flow enters the heated section. We then evaluate local

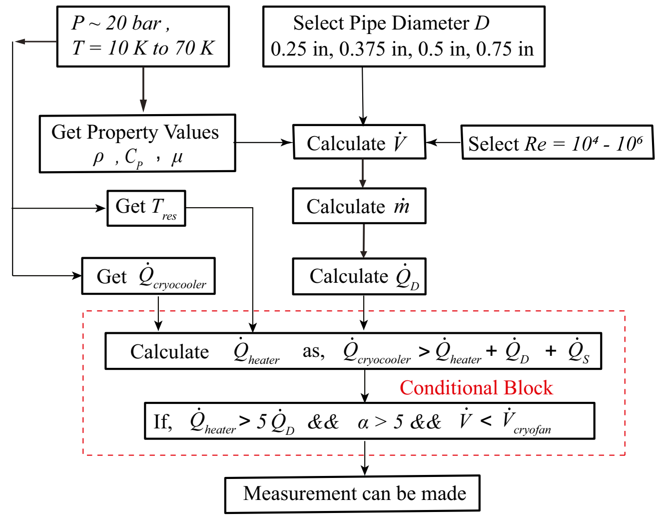

Fig. 3. Flowchart of the design and feasibility analysis used to determine an optimal circulation-loop geometry and operating envelope for heat-transfer measurements under the imposed hardware and metrology constraints.

heat-transfer coefficients at $x_1 = 20D$ and $x_2 = 40D$, and the flow exits the heated section at $x = 50D$. Including the return leg (where the flow is conduction-cooled through a thermal strap anchored to the cryocooler), the total loop length is taken to be ∼ $100D$.

Following the flowchart in Fig. 3, we explore candidate diameters $D = 0.25, 0.325, 0.5, 0.75$ in. For a given D and operating conditions (P, T), we compute the volumetric flow rate $\dot{V}$ required to achieve a specified Reynolds number Re and verify that the selected cryofan can supply that flow, i.e., $\dot{V} \leq \dot{V}_{\text{cryofan}}$, where $\dot{V}_{\text{cryofan}}$ is the maximum volumetric flow rate (capacity) deliverable by the cryofan at the relevant operating pressure and temperature, taken from the manufacturer performance curve. The corresponding loop pressure drop produces a dissipative (frictional) heat load $\dot{Q}_D$, which must be removed by the cryocooler together with other thermal loads. The manufacturer performance curves for the PT420 and the cryofan are used in this analysis.

A measurement at a given (P, T, Re) is feasible only if four coupled constraints are satisfied. First, the cryocooler must be able to sustain steady inlet conditions while removing the total thermal load on the loop, i.e.,

$$\dot{Q}_{\text{heater}} + \dot{Q}_D + \dot{Q}_S \leq \dot{Q}_{\text{cryocooler}}(T) \tag{6}$$

where $\dot{Q}_{\text{heater}}$ is the applied heating power in the test section, $\dot{Q}_D$ is the dissipation associated with circulating the flow, and $\dot{Q}_S$ represents static parasitic loads (e.g., conduction from the cryofan body and residual radiative heating). Second, the applied heater power must dominate the frictional (drive) heating so that the inferred heat-transfer coefficient is controlled primarily by the known heat input rather than by uncertain dissipation; we enforce

$$\dot{Q}_{\text{heater}} \geq 5\dot{Q}_D \tag{7}$$

Third, the induced bulk-temperature rise across the heated section, $\Delta T = T_{b,\text{out}} - T_{b,\text{in}}$, must be resolvable by the thermometry; we require

$$\alpha \equiv \Delta T / \Delta T_{\text{res}}(T) \geq 5 \tag{8}$$

where $\Delta T_{\text{res}}(T)$ is the thermometer resolution at temperature T. Finally, the required volumetric flow rate must lie within the cryofan operating envelope, i.e.,

$$\dot{V} \leq \dot{V}_{\text{cryofan}} \tag{9}$$

For each candidate diameter D and operating temperature T, we determine the maximum Reynolds number permitted by each individual constraint, denoted Re_i, and define the attainable measurement ceiling as $Re_{\max} = \min(Re_i)$.

Following the flowchart in Fig. 3, we evaluate feasibility at three representative temperatures, T = 10 K, 40 K, and 80 K. For each temperature, we generate a set of four diagnostic plots for each diameter, shown in Figs. 4–6.

Panel (a) ($\dot{Q}_{\text{heater}}$ vs Re), corresponding to enforcing condition in Eq. (6), indicates how much heater power can be applied while remaining within the cryocooler heat-lift constraint after accounting for the loop dissipation. As the Reynolds number increases, the frictional dissipation $\dot{Q}_D$ grows rapidly. This "internal heating" consumes the fixed cooling capacity $\dot{Q}_{cryocooler}$, forcing $\dot{Q}_{heater}$ to trend toward zero at high Re. This represents the ultimate thermal ceiling of the system.

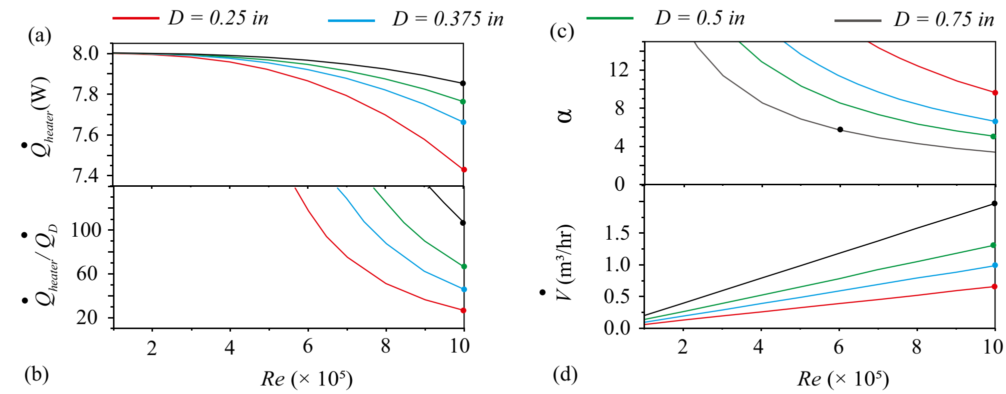

Fig. 4. Design-feasibility plots at T = 10 K for different circulation-loop diameters: (a) $\dot{Q}_{\text{heater}}$ vs Re, (b) $\dot{Q}_{\text{heater}}/\dot{Q}_D$ vs Re, (c) α vs Re, and (d) $\dot{V}$ vs Re. The circle markers indicate the limiting Reynolds number Re_i imposed by each feasibility constraint, and $Re_{\max} = \min(Re_i)$ sets the achievable measurement ceiling for a given diameter.

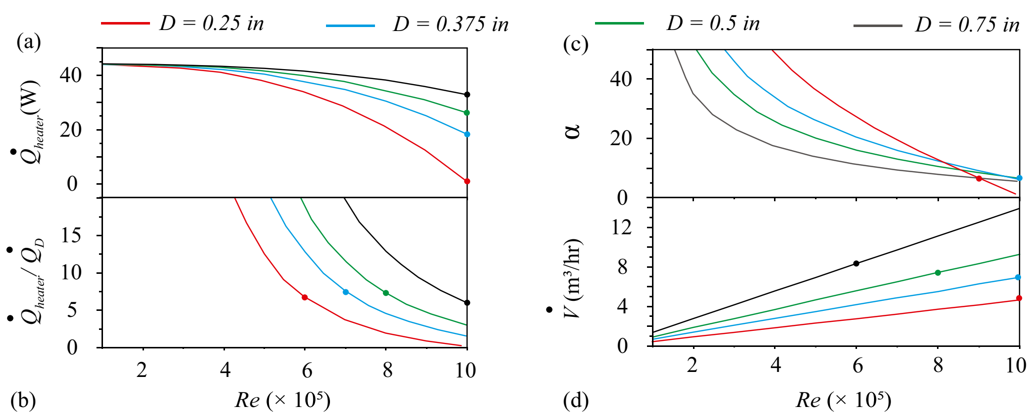

Fig. 5. Design-feasibility plots at T = 40 K for different circulation-loop diameters: (a) $\dot{Q}_{\text{heater}}$ vs Re, (b) $\dot{Q}_{\text{heater}}/\dot{Q}_D$ vs Re, (c) α vs Re, and (d) $\dot{V}$ vs Re. Circle markers indicate the limiting Reynolds number Re_i from each constraint, with $Re_{\max} = \min(Re_i)$.

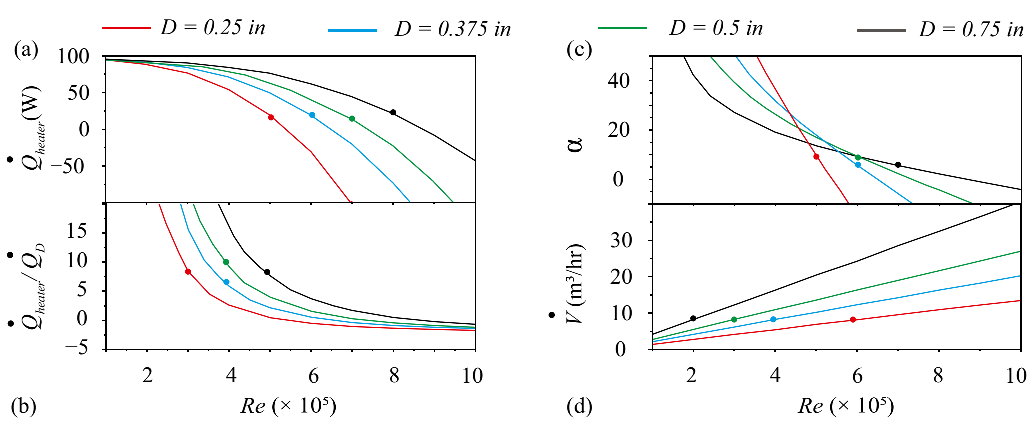

Fig. 6. Design-feasibility plots at T = 80 K for different circulation-loop diameters: (a) $\dot{Q}_{\text{heater}}$ vs Re, (b) $\dot{Q}_{\text{heater}}/\dot{Q}_D$ vs Re, (c) α vs Re, and (d) $\dot{V}$ vs Re. Circle markers indicate the limiting Reynolds number Re_i from each constraint, with $Re_{\max} = \min(Re_i)$.

Panel (b) ($\dot{Q}_{\text{heater}}/\dot{Q}_D$ vs Re), corresponding to enforcing condition in Eq. (7) quantifies how many times the applied heater power exceeds the frictional (drive) heating. At very high Re, the frictional dissipation becomes so large that the required applied power to maintain this ratio would exceed the cryocooler capacity, creating a mechanical limitation on the measurement validity.

Panel (c) (α vs Re), corresponding to enforcing condition in Eq. (8) shows the metrology margin $\alpha = \Delta T/\Delta T_{\text{res}}$, i.e., how many times the induced bulk temperature rise exceeds the thermometer resolution at that temperature. Accurate determination of h requires a bulk temperature rise ΔT that is significantly larger than the thermometer resolution: $\alpha = \Delta T/\Delta T_{res} \geq 5$. It shows that as Re (and thus mass flow $\dot{m}$) increases, the ΔT across the test section for a given $\dot{Q}_{heater}$ decreases ($\Delta T \propto \dot{Q}/\dot{m}C_p$). At high Re, α drops toward the threshold of 5, marking the resolution limit of the Cernox sensors.

Panel (d) ($\dot{V}$ vs Re), corresponding to enforcing condition in Eq. (9) gives the volumetric flow rate required to reach a given Reynolds number and must not exceed the cryofan capacity: $\dot{V} \leq \dot{V}_{cryofan}$. It shows the linear relationship between $\dot{V}$ and Re for each diameter, identifying where the Stirling cryofan reaches its maximum RPM.

The logical measurement ceiling, Re_{max}, is determined by the "bottleneck principle": it is the minimum Re value among these four individual constraint limits (Re_i), indicated by the circular markers in each panel. In each panel, the circular marker identifies the limiting Reynolds number Re_i associated with that constraint; the four panels therefore yield four values of Re_i, and the attainable ceiling for that diameter and temperature is then $Re_{\max} = \min(Re_i)$. This graphical approach makes it immediately clear which constraint is limiting in each operating regime and how design choices (particularly D) shift the achievable Re envelope.

The cryocooler-stage allocation is temperature dependent and enters directly through the cooling-capacity constraint in panel (a). At $T = 10$ K, the second-stage cold head (CH2) is used to cool the circulating supercritical helium, while the dominant static load from the cryofan body is intercepted on the first-stage cold head (CH1). With CH2 providing ~ 8 W at 10 K, the steady-state balance reduces to $\dot{Q}_{\text{heater}} + \dot{Q}_D \leq 8$ W, i.e., $\dot{Q}_{\text{heater}} \leq 8 - \dot{Q}_D$. The corresponding thermometer resolution is $\Delta T_{\text{res}} = 6$ mK [37], and the metrology constraint is enforced through $\alpha = \Delta T/\Delta T_{\text{res}} \geq 5$ at the mass flow rate associated with the chosen Re. At $T = 40$ K and 80 K, the loop is cooled by CH1, which provides substantially higher capacity in this range. For $T = 40$ K, we use $\dot{Q}_{\text{cryocooler}} = 50$ W and take $\dot{Q}_S = 6$ W, giving $\dot{Q}_{\text{heater}} \leq 50 - 6 - \dot{Q}_D$, with $\Delta T_{\text{res}} = 13$ mK at 40 K [37]. For $T = 80$ K, we use $\dot{Q}_{\text{cryocooler}} = 100$ W, giving $\dot{Q}_{\text{heater}} \leq 100 - 6 - \dot{Q}_D$, and $\Delta T_{\text{res}} = 16$ mK at 80 K [37]. Applying the same four-constraint procedure across temperatures yields the feasibility envelopes and the corresponding $Re_{\max}$ values summarized in Figs. 4–6, which are then used to select the loop diameter and operating strategy that maximize the accessible Reynolds-number range while maintaining robust measurement fidelity.

3. Optimized experimental setup

Fig. 7 summarizes the diameter trade study by plotting the maximum measurable Reynolds number $Re_{\max}$ as a function of temperature for each candidate circulation-loop inner diameter. Because the feasibility analysis is carried out at $T = 10$ K, 40 K, and 80 K, each diameter D yields three corresponding $Re_{\max}$ values; connecting these points provides a clear visualization of the Reynolds-number coverage achievable across the required temperature range for that loop size. The diameter that offers the highest overall $Re_{\max}(T)$ coverage is selected for the experiment. As shown in Fig. 7, $D = 0.5$ in provides the most favorable coverage across the full temperature window relevant to the heat-transfer measurements while remaining compatible with the cryocooler capacity, thermometry resolution, and cryofan flow capability. Based on the cryofan manufacturer performance curves, we verify that the Stirling Cryogenics Bohmwind cryofan can provide the required

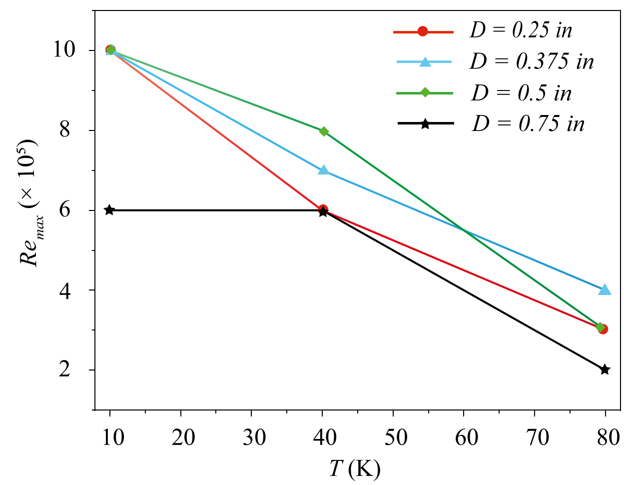

Fig. 7. Maximum Reynolds number $Re_{\max}$ achievable at different temperatures for several circulation-loop inner diameters. The selected $D = 0.5$ in loop provides the best overall Re coverage across the required temperature range.

volumetric-flow range $\dot{V}$ for the selected loop diameter $D = 0.5$ in over the targeted operating conditions; we therefore adopt this model for the experiment. Using a higher-capacity cryofan is not expected to substantially extend the accessible Reynolds-number range because $Re_{\max}$ is set primarily by the thermal and metrology constraints rather than by the cryofan flow ceiling.

The resulting experimental setup, designed and assembled at the National High Magnetic Field Laboratory, is shown in Fig. 8. The experimental setup implements several critical innovations to ensure the high Reynolds number capability is matched by high metrological precision and thermal stability. The experiment is housed in a 12 inch-bore cryostat with liquid-nitrogen (LN_2) jacket cooling and vacuum insulation (Fig. 8(a)). The main bore vacuum port evacuates the experimental space, while a dedicated annular-space vacuum port maintains vacuum in the insulating annulus. Separate LN_2 fill and vent ports service the nitrogen jacket to keep the surrounding walls near LN_2 temperature and thereby suppress radiative heat load to the insert.

The insert is supported by a top plate that seals to the cryostat and serves as the mechanical backbone of the system. The facility utilizes a Stirling Cryogenics Bohmwind cryofan, which features a high-precision balanced shaft and impeller designed with a cantilever architecture. This design is significant because it allows the electric motor to operate at ambient temperatures while the impeller remains at cryogenic temperatures, effectively avoiding the need for cold bearings that are prone to wear and thermal failure in high-speed applications. This configuration ensures a Mean Time Between Maintenance (MTBM) of over 20,000 hours, providing the reliability required for the long steady-state periods needed for supercritical fluid measurements. Refrigeration is provided by a Cryomech PT420 pulse-tube cryocooler, which provides a base temperature of 2.8 K and dual cooling capacities of 2.0 W @ 4.2 K and 55 W @ 45 K. Unlike standard Gifford-McMahon (GM) coolers, the pulse-tube architecture has no moving parts in the cold head, which drastically reduces mechanical vibration—a critical innovation for maintaining the stability of sensitive cryogenic pressure and temperature readings. The PT420 cryocooler and the cryofan are mounted on the top plate, and the circulation loop is closed by connecting the loop ends to the cryofan inlet and outlet using Swagelok VCR fittings, providing leak-tight operation up to 3000 psig (206 bar), which is an order of magnitude above the target 20 bar operating pressure. A VCR tee is incorporated at one connection to provide a high-pressure charging interface. Helium is charged into the loop via a 1/16-inch thin capillary, a design choice that minimizes the cross-sectional area for parasitic thermal conduction from the room-temperature top plate to the cryogenic

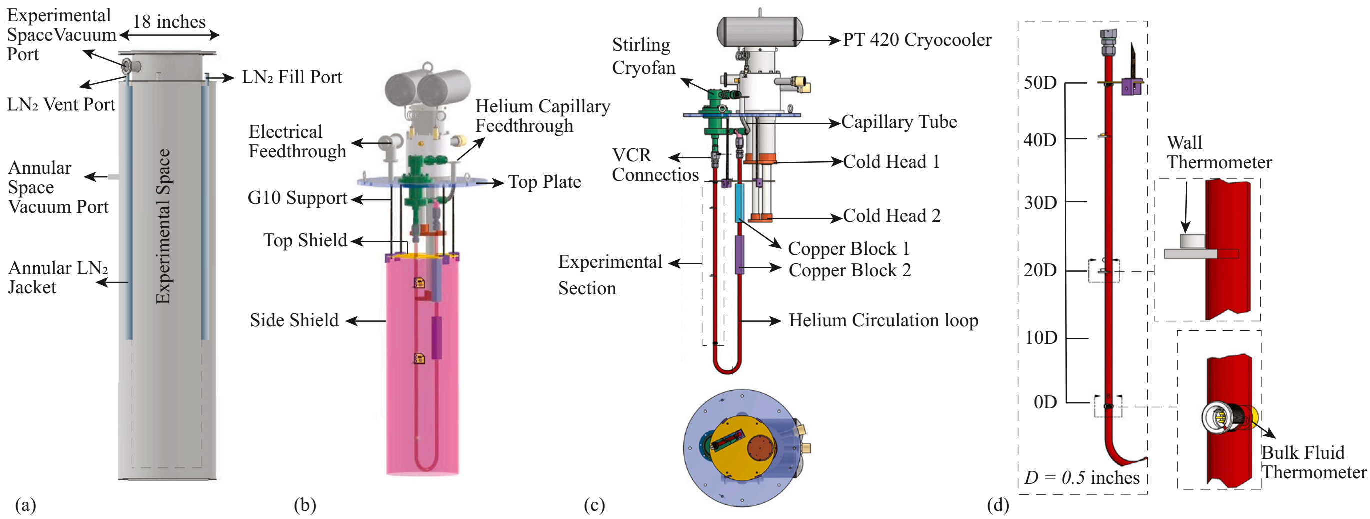

Fig. 8. Optimized experimental setup. (a) Vacuum-jacketed, LN_2-cooled cryostat that houses the insert. (b,c) Insert assembly highlighting the cryofan, cryocooler, and circulation loop. (d) Test-section instrumentation: bulk thermometers are located at $x = 0D$ and $x = 50D$, and wall thermometers at $x = 20D$ and $x = 40D$, where local heat-transfer coefficients are evaluated. Here $D = 0.5$ in is the selected loop inner diameter.

loop. The tee connects to a thin capillary fill line via VCR reducers and a VCR gland welded to the capillary, enabling reliable high-pressure sealing while allowing disconnection when needed. The capillary exits the cryostat through the top plate using a dedicated feedthrough implemented with a KF-40 to Ultra-Torr 1/16 in I.D. compression-port adapter.

The circulation loop comprises a heated test section and a cooling section. With $D = 0.5$ in, the test-section length is $L = 50D = 25$ in. A nichrome heater wire is tightly wound over the full test-section length to approximate a uniform heat-flux boundary condition and to deliver a well-defined heat input to the flowing SHe. To resolve the small temperature gradients characteristic of high-Re flows, the facility utilizes Cernox RTD sensors (CX-1050 series). These sensors were selected for their high sensitivity over the 4–80 K range and their long-term stability of ± 15 mK. Bulk fluid temperatures are measured at the test-section inlet ($x = 0D$) and outlet ($x = 50D$) using Cernox thermometers inserted into the flow. Each bulk sensor is mounted inside a copper bobbin attached to a G-10 standoff anchored to an electrical feedthrough, minimizing parasitic heat conduction from the feedthrough and ensuring that the sensor response tracks the bulk fluid rather than local solid temperatures. Local wall temperatures are measured at the heat-transfer evaluation locations ($x = 20D$ and $x = 40D$) using Cernox sensors mounted in custom copper clamps. These clamps include a curved, compliant copper contact that grips the tube to provide repeatable thermal contact; the thermometers are screw-mounted to the clamp to ensure stable positioning and low contact resistance.

The cooling section maintains the test-section inlet temperature by removing heat from the circulating helium through conduction to the cryocooler cold heads. Copper thermal intercept blocks are clamped to the loop, and flexible thermal straps couple the blocks to the cryocooler stages. The first-stage strap is used over the full operating range, while the second-stage strap is attached only for measurements at temperatures below ~ 10 K. Minimizing parasitic heat ingress is vital for maintaining the "dominated heat flux" boundary condition. To further suppress parasitic radiative heating, the insert incorporates two copper radiation shields. A top shield blocks radiation from the 300 K top plate and is supported by G-10 rods; it is cooled by the first-stage cold head via a thermal strap. A cylindrical side shield can be mounted to the top shield using copper brackets when additional radiative shielding is needed, particularly for sub-10 K operation; at higher temperatures the LN_2-jacketed cryostat already provides substantial radiative interception. Vacuum degree is maintained via separate ports for the main bore and insulating annulus, ensuring a stable environment where air pressure fluctuations (which can cause 1 mK shifts in boiling media) are suppressed below critical levels.

Temperature regulation and readout are implemented with dedicated heaters and distributed thermometry. Resistive trim heaters mounted on the cryocooler cold heads provide closed-loop control of the refrigeration delivered to the circulation loop, enabling stable control of the test-section inlet bulk temperature $T_{b,\mathrm{in}}$. Cernox thermometers are installed at key locations including the bulk inlet and outlet, wall-temperature stations, cryocooler cold heads, and radiation shields. All Cernox sensors are read out using a four-wire configuration to suppress lead-resistance errors. Sensor excitation is provided by a current source while voltages are recorded with an NI DAQ; the resistance-to-temperature conversion is performed in LabVIEW using the sensor calibration data. Heater leads and sensor leads are routed through a top-plate electrical feedthrough implemented as a tee with two Amphenol connectors, separating high-current heater wiring from low-level sensor wiring to reduce electrical cross-talk and improve measurement robustness. The test-section heater is powered by a current source that also records the delivered electrical power, providing the input needed for heat-flux and energy-balance calculations.

Finally, the helium charging, purging, and pressure-control hardware is implemented as a dedicated transfer and regulation system shown in Fig. 9. The external manifold is constructed from stainless-steel components using high-pressure Swagelok VCR connections (glands, nuts, and metal gaskets) and ball valves, providing leak-tight operation up to ~ 3000 psig, well above the maximum operating pressure of 25 bar. A pressure gauge provides continuous monitoring of loop pressure, and a relief valve set to 25 bar protects the system against accidental overpressure. Charging is performed by opening the valve V1 with V2–V4 closed; depressurization is achieved with V1 and V4 closed while V2 and V3 are opened; and evacuation of the loop is performed by opening V2 and V4 with V1 and V3 closed. Together with the cryofan-driven loop, cryocooler-based thermal control, and distributed thermometry described above, this charging and regulation system enables repeatable preparation of the loop (purge, fill, and pressure setpoint) and stable operation over the targeted pressure–temperature space. With the facility assembled and commissioned, we will conduct systematic forced-convection measurements of the supercritical-helium heat-transfer coefficient; the resulting dataset and its implications for

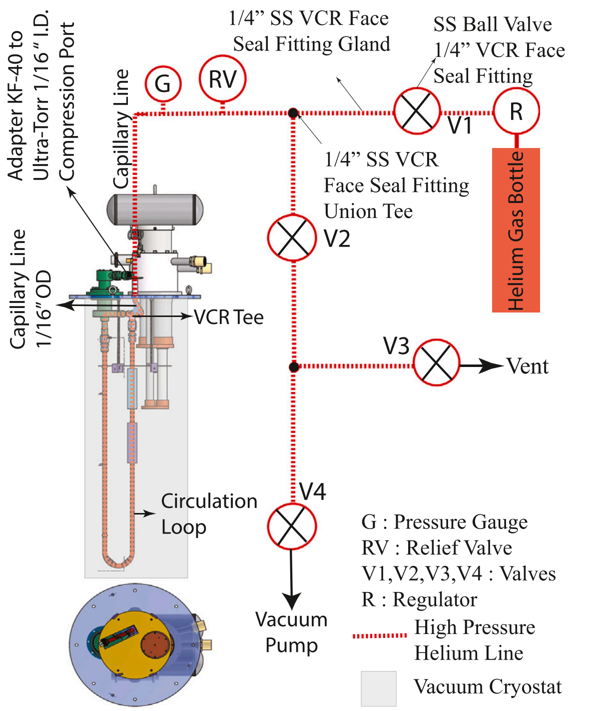

Fig. 9. Helium transfer and regulation system for charging, purging, and pressure control. A thin 1/16 in OD capillary feeds helium into the high-pressure circulation loop inside the cryostat vacuum space. The external manifold includes a pressure gauge, relief valve, ball valves, and regulator for safe operation and controlled fill/vent/vacuum procedures.

correlation validation and development will be reported in future publications.

4. Summary

In this work, we identify a critical gap in the forced-convection heat-transfer database for supercritical helium in the IZEA-relevant regime, which compels current heat-exchanger design to rely on correlations that are only weakly validated under the most demanding conditions. We address this need by translating the IZEA operating envelope into explicit facility requirements and developing a quantitative, constraint-driven design methodology that couples the flow objective (achievable Re set by loop diameter D and cryofan capacity $\dot{V}_{\mathrm{cryofan}}$) with the governing thermal and metrology limits, including cryocooler capacity $\dot{Q}_{\mathrm{cryocooler}}(T)$, parasitic heat load $\dot{Q}_S$, frictional dissipation $\dot{Q}_D$, and thermometer resolution T_{res}.

This integrated trade study delineates the feasible measurement space and the corresponding Re_{max} across temperature, leading to an optimized experimental implementation: a cryofan-driven closed SHe loop with a uniformly heated test section, distributed wall/bulk thermometry, conduction-cooled intercepts, and controlled shielding. The effective scope of application of the present methodology is governed by the coupled thermohydraulic and thermal constraints of cryogenic forced-flow helium systems. In particular, the finite cryocooler cooling power and the large circulation loop diameter required to achieve high Reynolds numbers impose a practical limitation toward relatively low steady-state heat fluxes. The results establish a quantitative design basis and a practical experimental platform for generating high-fidelity forced-convection heat-transfer data for supercritical helium in the IZEA-relevant operating space and beyond, thereby enabling correlation validation and reducing uncertainty in heat-exchanger design. While this paper establishes the facility design and defines the operational feasibility envelope, the first experimental dataset generated using this platform will be reported in a subsequent publication. The measurement approach and instrumentation have been designed to ensure high reliability and repeatability of the collected data. The forthcoming study will also include an assessment of measurement uncertainty and data reduction procedures to provide a transparent evaluation of the accuracy and confidence bounds of the reported results.

CRediT authorship contribution statement

Parmit S. Virdi: Writing – review & editing, Writing – original draft, Methodology, Formal analysis. **Wei Guo:** Writing – review & editing, Writing – original draft, Supervision, Resources, Project administration, Methodology, Funding acquisition, Formal analysis, Conceptualization. **Louis N. Cattafesta III:** Writing – review & editing, Funding acquisition. **Peter Cheetham:** Writing – review & editing, Funding acquisition. **Lance Cooley:** Writing – review & editing, Funding acquisition. **Jonathan C. Gladin:** Writing – review & editing, Funding acquisition. **Jiangbiao He:** Writing – review & editing, Funding acquisition. **Chul Kim:** Writing – review & editing, Funding acquisition. **Hui Li:** Writing – review & editing, Funding acquisition. **Juan Ordonez:** Writing – review & editing, Funding acquisition. **Sastry Pamidi:** Writing – review & editing, Funding acquisition. **Jian-Ping Zheng:** Writing – review & editing, Funding acquisition.

Declaration of competing interest

The authors declare the following financial interests/personal relationships which may be considered as potential competing interests:

Wei Guo reports that financial support was provided by NASA. Wei Guo also reports that financial support was provided by National Science Foundation. If there are other authors, they declare that they have no known competing financial interests or personal relationships that could have appeared to influence the work reported in this paper.

Acknowledgments

The authors acknowledge the support from NASA under award 80NSSC22M0068. The work was conducted at the National High Magnetic Field Laboratory at Florida State University, which is supported by the National Science Foundation Cooperative Agreement No. DMR-2128556 and the State of Florida.

Data availability

Data will be made available on request.

References

[1] Green MA. Cooling intrinsically stable superconducting magnets with supercritical helium. IEEE Trans Nucl Sci 1971;18:669–70. https://doi.org/10.1109/TNS.1971.4326147
[2] Michael PC, Golfinopoulos T, Kaplan A, Schweiger S, Garcia I, Watterson A, Chamberlain S, Nash D, Craighill C, Sanabria C, Laamanen E, McCormack C. Supercritical helium flow calorimetry at the MIT superconducting magnet test facility. IEEE Trans Appl Supercond 2025;35:1–6. https://doi.org/10.1109/TASC.2024.3508664
[3] Hoenig M, Montgomery D. Dense supercritical-helium cooled superconductors for large high field stabilized magnets. IEEE Trans Magn 1975;11:569–72. https://doi.org/10.1109/TMAG.1975.1058601
[4] Barber J, Brisson J, Minervini J. Forced flow cooling of high field, rebco-based, fusion magnets using supercritical hydrogen, helium, and neon. Cryogenics 2018;96:34–43. https://doi.org/10.1016/j.cryogenics.2018.10.005
[5] Pamidi S, Kim CH, Graber L, High-temperature superconducting (HTS) power cables cooled by helium gas. In: Superconductors in the power grid. Elsevier; 2015. p. 225–60.
[6] Souza JA, Ordonez JC, Hovsapian R, Vargas JVC. Thermal modeling of helium cooled high-temperature superconducting DC transmission cable. IEEE Trans Appl Supercond 2011;21:947–52.
[7] Ordonez JC, Souza JA, Shah DR, Vargas JVC, Hovsapian R. Temperature and pressure drop model for gaseous helium cooled superconducting DC cables. IEEE Trans Appl Supercond 2013;23:5402005.
[8] Miller J, Lue J, Shen S, Lottin J. Measurements of stability of cabled superconductors cooled by flowing supercritical helium. IEEE Trans Magn 1979;15:351–4.

[9] Martinez A, Duchateau J-L, Mardion GB, Gauthier A, Rousset B. Supercritical helium cooling of a cable in conduit conductor with an inner tube. Cryogenics 1994;34:591–4.

[10] Wachi Y, Ono M, Hamajima T. Heat transfer characteristics of the supercritical helium in a cable-in-conduit conductor. IEEE Trans Appl Supercond 1995;5:568–71.

[11] Virdi PS, Guo W, Cattafesta III LN, Cheetham P, Cooley L, Gladin JC, He J, Kim C, Li H, Ordonez J, et al. Liquid hydrogen storage, thermal management, and transfer-control system for integrated zero emission aviation (izea). Appl Energy 2025;393:126054.

[12] Giarratano PJ, Arp VD, Smith RV. Forced convection heat transfer to supercritical helium. Cryogenics 1971;11:385–93.

[13] Giarratano PJ, Jones MC. Deterioration of heat transfer to supercritical helium at 2· 5 atmospheres. Int J Heat Mass Transf 1975;18:649–53.

[14] Ogata H, Sato S. Forced convection heat transfer to supercritical helium. TEION KOGAKU (Journal of Cryogenics and Superconductivity Society of Japan) 1972;7:20–8.

[15] Pron'ko VG, Malyshev GP. Heat transfer in the turbulent flow of helium at supercritical pressure in tubes of small diameter. Teplofiz. Vys. Temp. 1972;10:1039–42.

[16] Brassington DJ, Cairns DNH. Measurements of forced convective heat transfer to supercritical helium. Int J Heat Mass Transf 1977;20:207–14.

[17] Yeroshenko VM, Kuznetsov YV, Shevchenko OA, Hendricks RC, Daney D. Measurements of mixed convective heat transfer to low temperature helium in a horizontal channel. Technical Report; 1979.

[18] Valyuzhinich MA, Vostrikov SN, Eroshenko VM, Kuznetsov EV, Shevchenko OA. Heat transfer on the middle generatrix of a horizontal pipe in the turbulent flow of low-temperature helium. Journal of engineering physics 1984;46:247–52.

[19] Dolgoy ML, Kirichenko YA, Sklovsky YB, Troyanov AM, Chernyakov PS. Heat transfer to near-critical helium in horizontal channels. Cryogenics 1983;23:125–6.

[20] Pioro I, Mokry S. Heat transfer to fluids at supercritical pressures. Heat Transfer: Theoretical Analysis, Experimental Investigations and Industrial Systems 2011:481–504.

[21] Munson B, Young D, Okiishi T. Fundamentals of fluid mechanics wiley; 1995.

[22] Pron'ko VG, Malyshev GP, Migalinskaya LN. Modes of “normal” and “deteriorated” heat exchange in the single-phase near-critical region in the turbulent flow of helium in tubes. Journal of engineering physics 1976;30:389–94.

[23] Brassington DJ. Prediction of heat transfer to supercritical helium at high heat fluxes using non-bulk values of pr and RE. Int J Heat Mass Transf 1978;21:76–7.

[24] Bogachev VA, Eroshenko VM, Yaskin L. Relative increase in heat transfer in viscous-inertial regimes of flow of helium at supercritical pressure in a heated pipe. Journal of engineering physics 1983;44:363–6.

[25] Bogachev VA, Yeroshenko VM, Snyitina OF, Yaskin L. Measurements of heat transfer to supercritical helium in vertical tubes under forced and mixed convection conditions. Cryogenics 1985;25:198–201.

[26] Yeroshenko VM, Yaskin L. Applicability of various correlations for the prediction of turbulent heat transfer of supercritical helium. Cryogenics 1981;21:94–6.

[27] Yaskin L, Jones MC, Yeroshenko VM, Giarratano PJ, Arp VD. A correlation for heat transfer to superphysical helium in turbulent flow in small channels. Cryogenics 1977;17:549–52.

[28] Liao SM, Zhao TS. Measurements of heat transfer coefficients from supercritical carbon dioxide flowing in horizontal mini/micro channels. J Heat Transf 2002;124:413–20. https://doi.org/10.1115/1.1423906

[29] Dang C, Hihara E. In-tube cooling heat transfer of supercritical carbon dioxide. Part 1. Experimental measurement. Int J Refrig 2004;27:736–47.

[30] Pitla SS, Robinson DM, Groll EA, Ramadhyani S. Heat transfer from supercritical carbon dioxide in tube flow: a critical review. HVACR Res 1998;4:281–301.

[31] Xia C, Wu L, Ni M, Hua T, Wang C. Heat transfer characteristics and correlation of supercritical hydrogen flow in vertical tubes: a numerical investigation. Appl Sci 2026;16. https://doi.org/10.3390/app16041972. https://www.mdpi.com/2076-3417/16/4/1972.

[32] Hendricks RC. Experimental heat-transfer results for cryogenic hydrogen flowing in tubes at subcritical and supercritical pressures to 800 pounds per square inch absolute. National Aeronautics and Space Administration; 1966.

[33] Locke J, Landrum B. Uncertainty analysis of heat transfer to supercritical hydrogen in cooling channels. In: 41st AIAA/ASME/SAE/ASEE joint propulsion conference & exhibit; 2005. p. 4303.

[34] Locke JM, Landrum DB. Study of heat transfer correlations for supercritical hydrogen in regenerative cooling channels. J Propuls Power 2008;24:94–103.

[35] Bluefors. Cryocooler, n.d.,,https://bluefors.com [Accessed: 5 August 2025].

[36] Cryogenic fans, n.d.,,https://stirlingcryogenics.com [Accessed: 5 August 2025].

[37] Cernox, n.d.,,https://www.lakeshore.com [Accessed: 9 September 2025].